Journal of Materials Chemistry C

PAPER

View Article Online
View Journal | View Issue

Cite this: J. Mater. Chem. C, 2019, 7, 1228

Monitoring the crystal orientation of black-arsenic *via* vibrational spectra†

A. Kandemir, [a] F. Iyikanat [b] and H. Sahin *[cd]

Received 12th October 2018,
Accepted 17th December 2018

DOI: 10.1039/c8tc05167d

rsc.li/materials-c

In this study, the structural, mechanical, and vibrational properties of a recently discovered anisotropic ultra-thin material, black-arsenic (b-As), are investigated by using density functional theory. Direction dependent elastic constants such as in-plane stiffness, Young's modulus and Poisson's ratio of single-layer b-As are calculated and compared with those of the structural cousin black-phosphorus (b-P). The calculated Poisson's ratio of b-As for the zigzag direction is nearly 1, which is quite higher than that of b-P, 0.65. Besides, it is found that all the three elastic constants are highly anisotropic and their values in the zigzag direction are almost three times higher than that of the armchair direction. The mechanical strength of the material is also calculated and high-toughness is seen in both armchair and zigzag directions. It is revealed that the material is quite stiff against straining along the zigzag direction; in contrast, it is quite flexible along the armchair direction. Vibrational stability analysis shows that the material is stable up to 9% biaxially applied strain, and 12% and 45% uniaxially applied strain in the zigzag and armchair directions, respectively. Furthermore, the prominent Raman active peaks of the b-As structure show strong anisotropy in the strain dependent vibrational spectra and they can also be used for easy-determination of the crystal orientation of b-As from Raman measurements.

I. Introduction

Since the successful isolation of single layer graphite,[1,2] two-dimensional (2D) materials have drawn extraordinary attention in the last decade. Following this, syntheses of novel 2D materials such as hexagonal boron nitride (h-BN),[3–5] silicene,[6,7] germanene,[6,8] transition metal dichalcogenides (TMDs),[9–15] stanene,[16,17] and phosphorene[18–20] have been accelerated owing to their wide range of features.

Elemental phosphorus, which is a nonmetal and thermodynamically stable, can exist in several polytypes classified loosely into three allotropes: white, red and black.[21] The low-dimensional molecular structures (zero-dimensional white phosphorus and one-dimensional white phosphorus nanorods), the layered structures (2D black phosphorus sheets), and the tubular structures (layered or bulk crystalline forms of red phosphorus) contain covalent structure motifs that are interconnected by van der Waals interactions.[22] Black phosphorus (b-P) was renominated as one of the best candidates in the 2D material family due to its fascinating properties such as layer-controlled band gap,[23,24] high electronic mobility,[25,26] and especially anisotropic features.[23,27–30] Because of its puckered hexagonal structure, b-P has planar two non-equivalent directions, armchair (Arm) and zigzag (ZZ), which allows 2D b-P crystals to show highly anisotropic properties.

A counterpart of b-P, a puckered hexagonal phase of As, black-arsenic (b-As), was recently discovered as a layered semiconductor 2D material.[31] However, more stable phases of ultra-thin arsenic structure, rhombohedral structure of As (r-As), were studied intensively during the recent years.[32–36] Simple methods such as the shear exfoliation method are used to obtain r-As nanosheets as in the work of Gusmao *et al.*, who have produced 2D r-As for electrochemical applications using kitchen blenders.[37] r-As is known as the only pure 2D stable phase, however; synthesis and identification of 2D b-As were questioned whether it is possible or fiction as thermodynamical basics.[38] They proposed that b-As can be obtained only with a high amount of impurities. However, as mentioned, kinetically controlled synthesis methods can make the achieving of pure b-As possible. In addition, computational studies revealed that application of out-of-plane strain can lead to a transition from an indirect bandgap semiconductor to a metal.[39] The existence of Dirac states is predicted in the strained phase of monolayer b-As.[40] Moreover, it was shown that b-As has one order of magnitude higher hole mobility compared to r-As; besides,

[a] Department of Materials Science and Engineering, Izmir Institute of Technology, 35430, Izmir, Turkey
[b] Department of Physics, Izmir Institute of Technology, 35430, Izmir, Turkey
[c] Department of Photonics, Izmir Institute of Technology, 35430, Izmir, Turkey. E-mail: hasansahin@iyte.edu.tr
[d] ICTP-ECAR Eurasian Center for Advanced Research, Izmir Institute of Technology, 35430, Izmir, Turkey

† Electronic supplementary information (ESI) available. See DOI: 10.1039/c8tc05167d

it was also predicted that b-As has an extremely high electron mobility of the same order as that of graphene and this feature shows direction dependency.[36] Thus, similar to anisotropic b-P, anisotropic b-As is a strong candidate for future developments of nanotechnology. In that case, poorly studied single layers of b-As are investigated mechanically and vibrationally, since the Raman response of b-P like materials has received significant attention due to its unusual features.[41,42]

In this paper, we present the structural, mechanical and vibrational properties of b-As. Specifically, we study the structural stability of b-As under strain by examining both vibrational and mechanical properties. Strain-dependent mechanical and vibrational properties are also shown to envision anisotropic behavior that can distinguish applied strain type; thus, vibrational spectra under three principal strain types are studied in detail. The rest of the paper is organized as follows: Computational methodology is given in Section II. The structural, mechanical and vibrational properties of b-As are presented in Section III. Strain-dependent vibrational properties of b-As are given in Section IV. Section V is devoted to conclusion of the results.

II. Computational methodology

First-principles calculations were carried out in the framework of density functional theory (DFT) using projector-augmented-wave (PAW) potentials and a plane-wave basis set as implemented in the Vienna *ab initio* simulation package (VASP).[43–45] The Perdew–Burke–Ernzerhof (PBE) form of the generalized gradient approximation (GGA) was adopted to describe the electron exchange and correlation.[46] The van der Waals (vdW) correction to the GGA functional was included by using the DFT-D2 method of Grimme.[47]

The energy cut-off value for the plane-wave basis set was taken to be 400 eV. Lattice constants and total energies were computed with the conjugate gradient method, where atomic forces and total energies were minimized. The convergence criterion for the energy was taken as 10^{-5} eV. The total force in the unit cell was reduced to a value of less than 10^{-4} eV Å^{-1}. In order to prevent interlayer interactions within the periodic images, we used a large vacuum spacing (at least 12 Å). Pressure on the unit cell was decreased to values less than 1 kB. The Γ centered k-point mesh scheme was adapted with a grid size of 12 × 9 × 1 for the structural relaxation calculations. All calculations were performed taking into account the spin-polarized case. The cohesive energy per atom was calculated using the formula

$$E_{\mathrm{Coh}} = [n_{\mathrm{As}}E_{\mathrm{As}} - E_{\mathrm{Str}}]/n_{\mathrm{As}} \quad (1)$$

where E_{As} and n_{As} are the isolated single atom energy of the As atom and the number of As atoms in the unit cell, respectively. E_{Str} stands for the total energy of the structure. The vibrational properties were obtained with the PHONOPY code,[48] which uses the force constants calculated with the finite-displacement method.[49]

III. Structural, vibrational and mechanical properties of single-layer b-As

Single-layer b-As has a puckered honeycomb structure consisting of two parallel layers of As atoms. Top and side views of the single-layer b-As are shown in Fig. 1(a). The optimized lattice parameters of the structure are a = 3.67 Å and b = 4.71 Å (see Table 1). The calculated lattice parameters agree well with previous theoretical results.[50] For comparison, previously calculated values of structural parameters of single-layer b-P are also given in Table 1. As expected, the lattice parameters of single-layer b-As are higher than those for single-layer b-P. Since the b/a ratio of b-As (1.28) is lower than that of b-P (1.38), slightly less anisotropy is expected in the properties of b-As. Each As atom in the crystal covalently bonds with 3 atoms, two in the same plane and one in a different plane. The bond length between As atoms in the same plane is d_1 = 2.50 Å, while

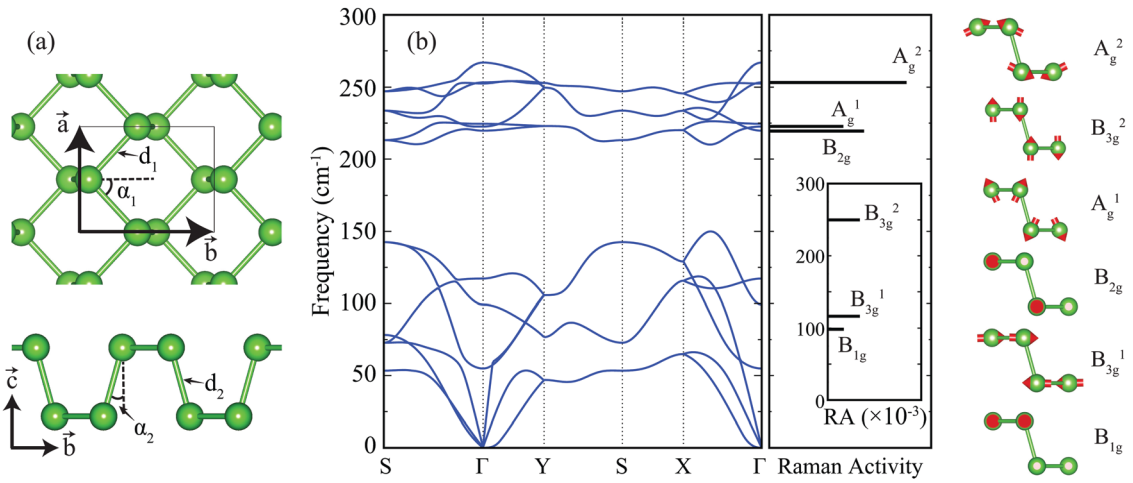

Fig. 1 (a) Top and side views of single-layer b-As. (b) Phonon-band structure and the corresponding Raman activity of b-As. The vibrational motion of As atoms in each phonon mode is shown in the right panel.

Table 1 The calculated parameters for the single-layer b-As structure are: the lattice constants, a and b; As–As distances, d_1 and d_2; As–As angles, α_1 and α_2; in-plane stiffness along zigzag and armchair directions, C_{ZZ} and C_{Arm}; the Young's modulus along zigzag and armchair directions, Y_{ZZ} and Y_{Arm}; Poisson's ratio along zigzag and armchair directions, ν_{ZZ} and ν_{Arm}

	a (Å)	b (Å)	$d_{1/2}$ (Å)	$\alpha_{1/2}$ (°)	$E_{Coh.}$ (eV)	$C_{ZZ/Arm}$ (N m^{-1})	$Y_{ZZ/Arm}$ (GPa)	$\nu_{ZZ/Arm}$
b-As	3.67	4.71	2.50	47.3	3.13	55.8	101.9	0.92
			2.48	15.4		19.6	35.8	0.33
b-P[29,51,52]	3.36	4.63	2.24	48.4	3.30	91	166	0.65
			2.26	21.4		29	44	0.21

the bond length between As atoms in different planes is d_2 = 2.48 Å. The thickness of the single-layer b-As, which is the vertical distance between atoms in different planes, is 2.39 Å. The bond angle between the atoms in the same plane is $\alpha_1 = 47.3^\circ$, while the angle between the bonds of the different plane atoms and the surface normal is $\alpha_2 = 15.4^\circ$. The cohesive energy per atom of single-layer b-As is calculated to be 3.13 eV, which is slightly less than the cohesive energy of single-layer b-P (see Table 1).

Fig. 1(b) presents the calculated phonon dispersion and vibrational characteristics of possible Raman-active modes of single-layer b-As. The unit cell of single-layer b-As consists of 4 atoms, and therefore the phonon dispersion of the crystal yields 3 acoustic and 9 optical modes. The force constant matrix is constructed by displacing atoms from their equilibrium positions in a 5 × 5 × 1 supercell. The calculated phonon dispersion curves exhibit real eigenvalues through all the symmetry points in the Brillouin Zone (BZ), confirming the dynamical stability of the single-layer b-As. Due to the heavier atomic masses, energies of phonon modes of single-layer b-As are significantly lower than that of the phonon modes of single-layer b-P.[53]

The vibrational motion of individual atoms in Raman active modes is shown in the right panel of Fig. 1(b). Since b-As has the same crystal structure as b-P, B_{1g}, B_{3g}^1, B_{3g}^2, A_g^1, A_g^2, and B_{2g} Raman-active modes observed in b-P are also seen in b-As.[56,57] B_{1g}, B_{3g}^1 and B_{3g}^2 modes have very low Raman intensities and their Raman activities are shown in the inset. The modes B_{1g} and B_{3g}^1 have in-plane vibrational character; while the motion of the atoms of B_{1g} is parallel to the zigzag direction, that of B_{3g}^1 is perpendicular to the zigzag direction. However B_{3g}^2 has out-of plane character. Previously, it was shown that only A_g^1, B_{2g} and A_g^2 modes are Raman-active in b-P with the frequencies of 365, 440, and 470 cm^{-1}, respectively.[53] Similarly, it is found that B_{2g}, A_g^1, and A_g^2 modes of b-As have much higher activities than the other modes with the frequencies of 219.5, 222.7, and 253.2 cm^{-1}, respectively. While the A_g^1 and A_g^2 modes have mixed in-plane and out-of-plane character, for the B_{2g} mode, As atoms in the zigzag chains exhibit counter-phase motion along the chain.

Since b-As has a puckered crystal structure, its mechanical properties are expected to exhibit anisotropy like b-P. Therefore, we examine the mechanical properties of single-layer b-As by calculating elastic constants for both the armchair and zigzag directions. A 3 × 3 supercell (containing 36 atoms) is used to determine the elastic constants of the material. By changing the lattice constants along the armchair and zigzag directions, the uniaxial strains ε_{Arm} and ε_{ZZ} are achieved ranging from −0.02 to 0.02 along each direction, with increment of the strain, 0.01. At each point, atomic positions are fully optimized. The strain energy is calculated from $E_S = E_T(\varepsilon) - E_T(\varepsilon = 0)$, where $E_T(\varepsilon)$ is the total energy of the strained material and $E_T(\varepsilon = 0)$ is the equilibrium total energy of the single-layer b-As. The strain energy is fitted to the formula $E_S = c_1\varepsilon_{ZZ}^2 + c_2\varepsilon_{Arm}^2 + c_3\varepsilon_{ZZ}\varepsilon_{Arm}$, and the c_1, c_2, and c_3 coefficients are determined.

The calculated in-plane stiffness, effective Young's modulus and Poisson's ratio are listed for zigzag and armchair directions in Table 1. The in-plane stiffness of the material along zigzag and armchair directions can be calculated by the formula $C_{ZZ} = (1/A_0)(2c_1 - c_3^2/2c_2)$ and $C_{Arm} = (1/A_0)(2c_2 - c_3^2/2c_1)$, where A_0 is the equilibrium area of the supercell. The stiffness values of the single-layer b-As along the two directions are found to be C_{ZZ} = 55.8 N m^{-1} and C_{Arm} = 19.6 N m^{-1}, which are almost half of that of b-P. Since the lattice constant of b-As is higher than that of b-P, the bond length between the atoms is longer and therefore b-As is less stiff than b-P. The effective Young's modulus of the material along zigzag Y_{ZZ} and armchair Y_{Arm} directions can be obtained from $Y_{ZZ} = C_{ZZ}/h_p$ and $Y_{Arm} = C_{Arm}/h_p$, respectively. Here, h_p is the effective thickness which is equal to the bulk interlayer spacing. The h_p value of bulk b-As is calculated to be 5.475 Å. The calculated Young's modulus values of the single-layer b-As are Y_{ZZ} = 101.9 GPa and Y_{Arm} = 35.8 GPa, which are very low compared to that of b-P. The Poisson's ratio of the single-layer b-As is also calculated. Poisson's ratio is the proportion of the transverse strain to the axial strain and can be defined as $\nu = -\varepsilon_{trans}/\varepsilon_{axial}$. The Poisson's ratio of the single-layer b-As is obtained from the formula $\nu_{ZZ} = c_3/2c_2$ and $\nu_{Arm} = c_3/2c_1$, for zigzag and armchair directions, respectively. The Poisson's ratio of the single-layer b-As in the zigzag and armchair directions is found to be ν_{ZZ} = 0.92 and ν_{Arm} = 0.33, respectively. It is worth noting that the Poisson's ratio along the zigzag direction is much higher than that of other 2D materials such as graphene, hBN, TMDs and even b-P.[54,57] Therefore, single-layer b-As is more sensitive to applied uniaxial strain than other 2D materials.

The strength of single-layer b-As is also investigated by applying biaxial and uniaxial strains. The stress curve of single-layer b-As is plotted as a function of the applied strain in Fig. 2(a). The ultimate strength is the stress value that reaches the maximum of the stress–strain curve. Beyond this point the material becomes unstable. As seen from the figure, stress–strain curves exhibit quite different behavior when the material is strained along zigzag and armchair directions. The ultimate strength along the armchair direction is considerably lower than that of the zigzag direction. It is found that the ultimate strengths are 7.77, 12.75, and 6.55 GPa with the corresponding strains of 13%, 21%, and 44% in the biaxially strained and uniaxially strained along zigzag and armchair directions, respectively. Thus, the ultimate strength values of single-layer b-As are lower than that of single-layer b-P (17.66 GPa and 7.56 GPa in the zigzag and armchair directions, respectively).[55] With the increase of strain along the zigzag direction, the stress curve shows a sudden decrease when it reaches the ultimate strength point. The structural deformation is non-reversible after

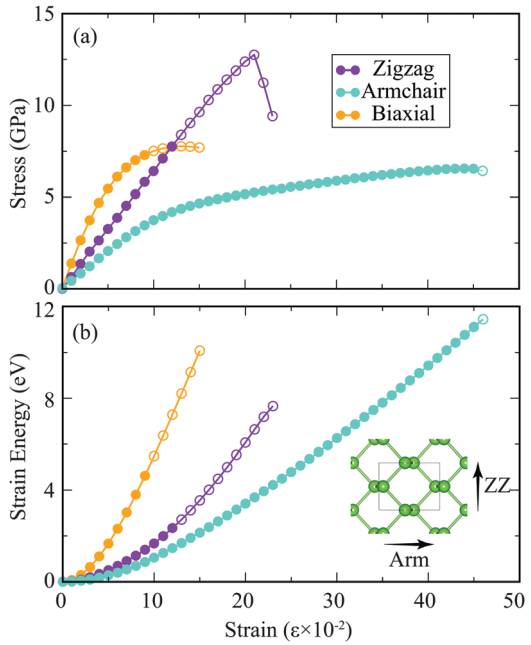

Fig. 2 The variation of (a) created stress and (b) strain energy with biaxial strain and uniaxial strain along armchair and zigzag directions. Shaded points indicate the dynamical instability.

this point. Therefore, single-layer b-As exhibits brittle property along the zigzag direction. In contrast, when the material is strained biaxially or uniaxially along the armchair direction, the stress curve smoothly passes the ultimate strength point. It is seen that single-layer b-As can sustain tensile strain up to 45% in the armchair direction. As a consequence of a highly puckered structure, single-layer b-As has a higher tensile tolerance compared to single-layer b-P.[29] It is worth mentioning that the stress–strain curve of the uniaxially strained material along the zigzag direction shows linear behavior, whereas when the material is strained biaxially or uniaxially along the armchair direction stress–strain curves exhibit parabolic behavior. Moreover, the strain energy *versus* applied strain is also plotted in Fig. 2(b). Strain energy curves show increasing behavior with the strains in the range 0–15%, 0–23%, and 0–46% for the material biaxially strained and uniaxially strained along zigzag and armchair directions, respectively.

In order to discuss the dynamical stability of single-layer b-As under strain, the phonon band dispersion of each strained case is also calculated. Fig. 3 shows phonon band dispersions of the 9%, 12%, and 45% biaxially strained structure and uniaxially strained structure along zigzag and armchair directions, respectively. Our calculations reveal that beyond these points phonon band dispersions of single-layer b-As exhibit imaginary phonon modes, which are indication of instability of the crystal under corresponding strains. As the applied strain along each direction increases the unstable region in the BZ increases. Top and side view geometries, and d_1, d_2, α_1, and α_2 values of strained materials are also shown in the right panel of Fig. 3. It is clearly seen that while in-plane and out-of-plane bond distances and angles change, applied strains lead to

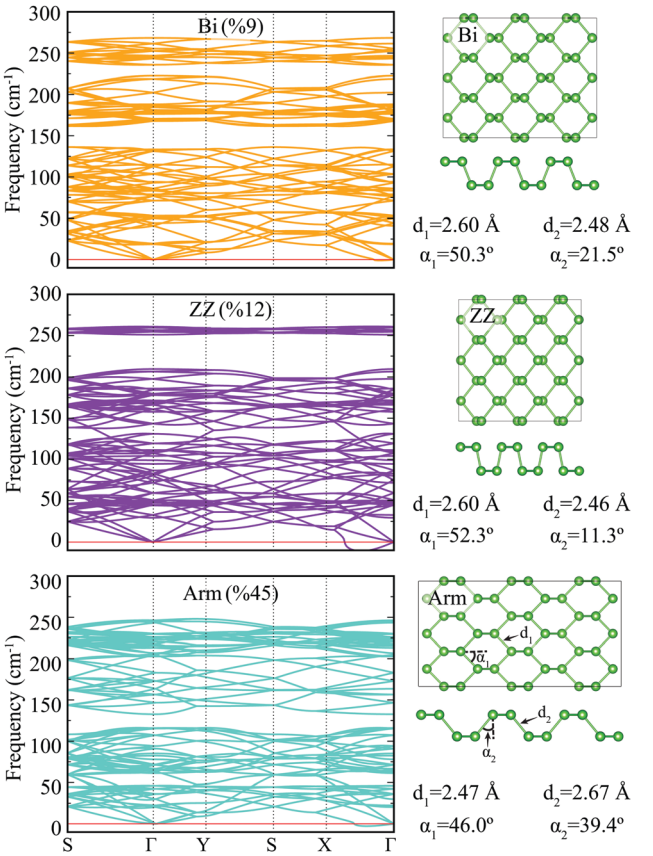

Fig. 3 Phonon band dispersions for single-layer b-As at 9% biaxial strain, and 12% and 45% uniaxial strains along zigzag and armchair directions, respectively. Dynamical instability stems from the imaginary eigenfrequencies between the *X* and *Γ* points.

insignificant structural reconstructions in the material until these points.

IV. The vibrational characteristics of single-layer b-As under applied fine-strain

A. Raman activity

Raman measurement is based on the interaction of photons and material, and thus, the Raman spectrum of a material can be sketched from the frequency based dispersion of the collected instantly scattered photons. Placzek's classical theory of polarizability can help to obtain the Raman spectrum of a material computationally. According to the theory, since the polarizability of a material is calculated, the Raman activity of a mode can be achieved by using the following equation:[57,58]

$$R_A = 45\tilde{\alpha}^2 + 7\beta \quad (2)$$

where $\tilde{\alpha}^2$ and β are isotropic and anisotropic parts of the derivative of polarizability tensor, respectively. In this formula, parameters and also Raman activity are invariant under the orientation of the sample and independent of the wavelength of exciting photons. With this simple and valid method, the

characteristic properties of the Raman active modes can be discussed and identified. The calculated Raman activity of the phononic modes of a material gives information about the vibrational properties of the material.

The vibrational properties of an ultra-thin material are vital for both detection and characterization of the material. As one of the widely used techniques, Raman spectroscopy allows one to differentiate ultra-thin materials at the characterization stage. Due to technological developments, during the measurement, external forces can be applied on ultra-thin materials and their responses also allow one to determine distinguishable features of those materials. The effect of strain on ultra-thin materials has been studied extensively in the last few decades.[59,60]

In this part, we investigate fine-strain response of the soft b-As single-layer. There are three main strain directions in two-dimensional materials like graphene, TMDs and b-P/b-As. Therefore, fine-strain effects on the vibrational properties of b-As along biaxial, zigzag and armchair directions are investigated and the change in both Raman activity and eigenfrequency of the prominent peaks between 0.5% compressive and 0.5% tensile strain is shown in Fig. 4.

As seen in Fig. 4(a), all the optical modes B_{2g}, A_g^1 and A_g^2 show phonon hardening (softening) under compressive (tensile) strain. It is calculated that the rate of change in eigenfrequencies as a function of applied external biaxial strain is 1.99, 1.53 and 0.46 cm^{-1}/strain for the modes B_{2g}, A_g^1 and A_g^2, respectively. Although they show the same trend in eigenfrequency change, different trends are seen with respect to Raman activity. The A_g^1 and A_g^2 modes show a sudden increase under compressive strain, whereas the mode B_{2g} shows a slow decrease in the Raman activity.

The effect of strain along armchair on the Raman activity of b-As is shown in Fig. 4(b). In this case, only the A_g^1 mode shows phonon hardening under compressive strain. On the other hand, the A_g^2 mode shows gradual phonon softening while compressive strain is applied. The most significant result is found in the optical mode B_{2g}, because that mode is inactive to the armchair type fine-strain and shows no change in eigenfrequencies. Due to the vibrational character of B_{2g}, which vibrates only along the zigzag in-plane direction (see Fig. 1), armchair type strain has no effect on this optical mode. The rate of change along armchair strain is calculated to be 0.04, 0.96 and −0.14 cm^{-1}/strain for the modes B_{2g}, A_g^1 and A_g^2, respectively. The same trends are seen in the Raman activity and all the modes show an increase under compressive strain.

Fig. 4(c) shows the strain effect on the Raman activity of b-As along the zigzag direction. As in the biaxial case, all the optical

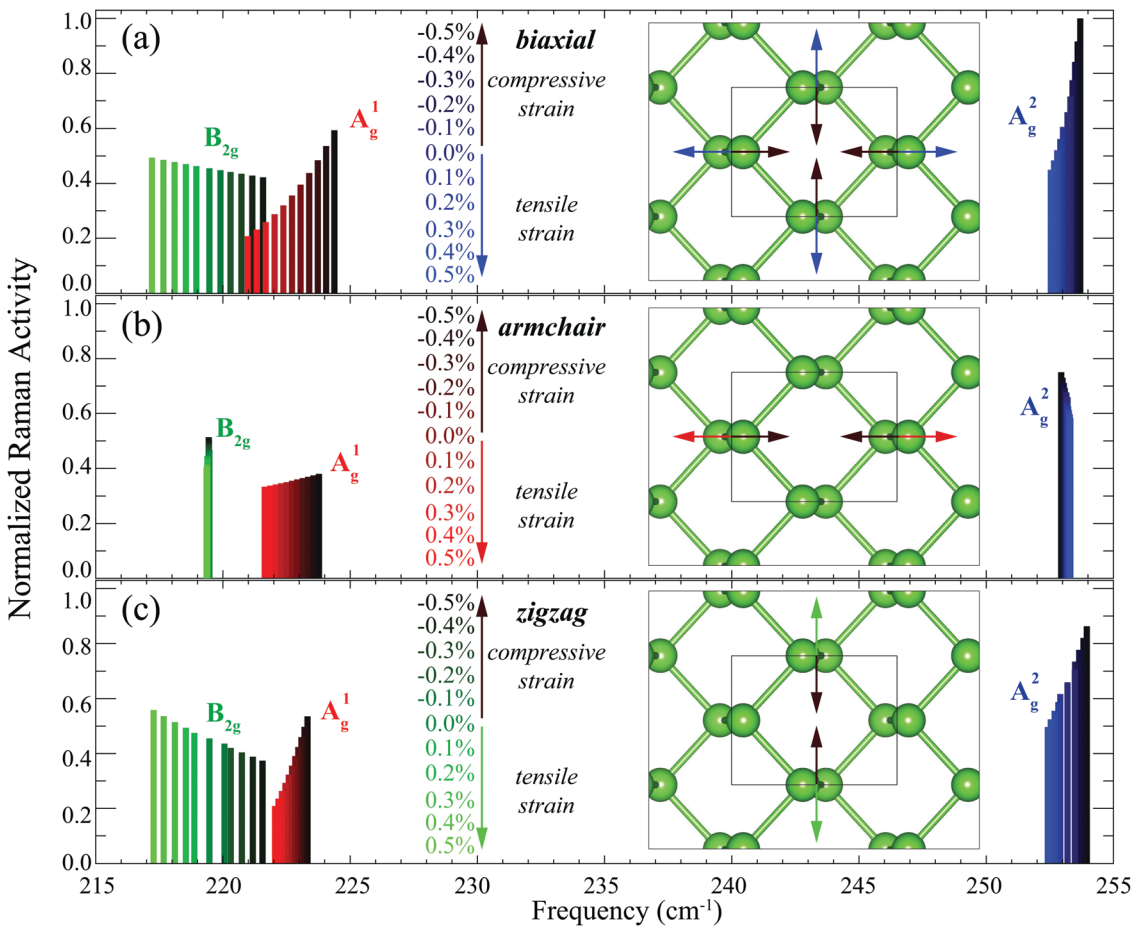

Fig. 4 Calculated Raman spectra of strained b-As single-layers along (a) biaxial, (b) armchair and (c) zigzag directions. Applied strain values are between −0.5 and 0.5 percentage. All Raman activity values are normalized with respect to the highest Raman active value.

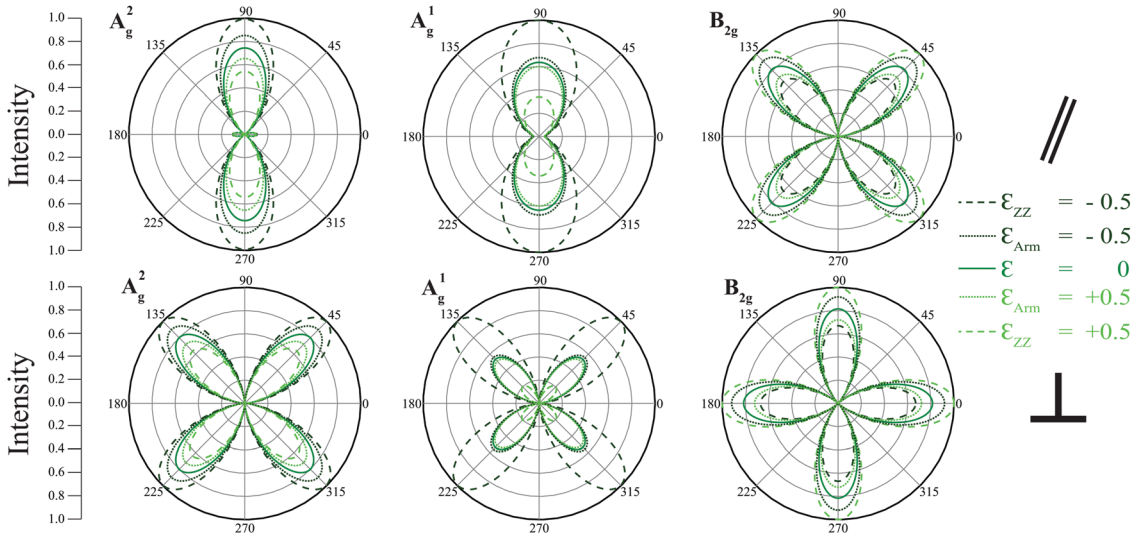

Fig. 5 Calculated angle dependent Raman spectra of b-As single-layers in parallel and cross-polarization configurations. Unstrained, the lowest and highest strained (along armchair and zigzag direction) structures are used. Each graph is normalized individually.

modes B_{2g}, A_g^1 and A_g^2 show phonon hardening (softening) under compressive (tensile) strain. However, the calculated rate of change for eigenfrequencies with respect to the applied zigzag strain differs and is found to be 1.95, 0.57 and 0.60 cm^{-1}/strain for the modes B_{2g}, A_g^1 and A_g^2, respectively. In contrast to the armchair direction in which the B_{2g} mode is inactive, the in-plane mode A_g^2 that vibrates along the armchair direction shows phonon hardening under compressive zigzag strain. This behavior can be explained with the effect of Poisson's ratio of the zigzag direction. It is seen that the major contribution for the effect of strain on the Raman activity of the optical modes of b-As comes from the zigzag direction. Compared to the other cases, the Raman activity change in the optical mode B_{2g} is more clear in this type of strain and the A_g^1 and A_g^2 modes show a sudden increase under compressive strain.

B. Angle-dependent and polarized Raman activity

To reveal the effect of strain and possible direction dependency, we investigated angle-dependent and polarized Raman activities of b-As single-layers. Fig. 5 shows parallel and cross polarized polar plots of the normalized Raman intensity as a function of angle for the A_g^2, A_g^1 and B_{2g} optical modes, respectively. For parallel and cross type angular dependence configuration of the Raman activity, scattering intensity is calculated with the methodology that is used in the work of Ribeiro *et al.*[41] related to angular dependence of the Raman response in b-P. Since our lattice vectors, *a* and *b*, are along the zigzag and armchair directions, respectively, the vector $[\cos\theta\ \sin\theta\ 0]$ is used for the incident beam. For parallel scattered light $[\cos\theta\ \sin\theta\ 0]$ and for cross scattered light $[-\sin\theta\ \cos\theta\ 0]$ are used.

As shown in Fig. 5, the representative Raman polar plots reveal distinguishable schematics for all modes. In parallel polarized configuration, A_g^2 and A_g^1 modes show the maximum peak at 90 and 270 degrees and have two-fold symmetry. However, A_g^2 and A_g^1 differ from each other since A_g^2 has the local maxima at 0 and 180 degrees and A_g^1 has no local maxima. With a strong difference, B_{2g} exhibits four-fold symmetry around each 45 degree of the four main regions of the *x*–*y* axis. In cross polarized configuration, all modes show four-fold symmetry. Compared to parallel polarized configuration, B_{2g} exhibits four-fold symmetry shifted 45 degrees. On the other hand, A_g^2 and A_g^1 rely on each 45 degree of the four regions.

In addition, strain effects on the Raman polar plots for the three prominent peaks are apparent if one compares each mode. For the three optical modes, the strain effect along the zigzag direction show a major change at fold symmetry points. On the other hand, the strain effect along the armchair direction shows a major change in A_g^2 and B_{2g} modes, but it shows an incommensurable change in the A_g^1 mode as previously mentioned. Besides, in parallel polarized configuration A_g^2 and A_g^1 modes have indistinguishable representation at 0 and 180 degrees.

V. Conclusions

In summary, by performing density functional theory-based calculations, we studied the structural, mechanical, and vibrational properties of recently discovered single-layer b-As. Our results revealed that the calculated elastic constants of b-As are highly anisotropic similar to the case of b-P. The calculated Poisson's ratio of b-As for the zigzag direction is nearly 1 and elastic constants along this direction are 3 times higher than that of the armchair direction. It was found that the in-plane stiffness and Young's modulus values of b-As are smaller than that of b-P, whereas the Poisson's ratio of b-As is larger than that of b-P. Stress–strain curves showed that the ultimate strength along the zigzag direction is considerably higher than that along the armchair direction. Therefore, the zigzag direction is more stiff than the armchair direction. On the other hand the armchair direction has quite high strain tolerance

compared to the other directions. Phonon calculations showed that single-layer b-As is no longer dynamically stable after 12%, 45%, and 9% applied strain for zigzag, armchair and biaxial directions, respectively.

In addition, strain dependent Raman spectra of b-As were investigated along biaxial and uniaxial directions. It was seen that prominent Raman-active modes behave completely differently in zigzag and armchair directions. Especially, it was found that the B_{2g} optical mode shows a negligible change in both Raman activity and eigenfrequency for ultra-fine strain along the armchair direction, whereas it strongly changes in the zigzag direction. Therefore, under applied uniaxial strain, the changes in both Raman activity and eigenfrequency shift point out the crystal orientation of b-As. Moreover, the angular dependence of Raman intensity of the prominent Raman-active modes was also shown. It was found that, under strain and polarization, the Raman fingerprints for b-As allow one to determine crystal orientation and distinguish prominent Raman active modes.

Conflicts of interest

There are no conflicts to declare.

Acknowledgements

Computational resources were provided by TUBITAK ULAKBIM, High Performance and Grid Computing Center (TR-Grid e-Infrastructure). HS acknowledges financial support from the GEBİP program of Türkiye Bilimler Akademisi-Turkish Academy of Sciences.

References

1 K. S. Novoselov, A. K. Geim, S. V. Morozov, D. Jiang, Y. Zhang, S. V. Dubonos, I. V. Grigorieva and A. A. Firsov, Electric Field Effect in Atomically Thin Carbon Films, *Science*, 2004, **306**, 666.
2 A. K. Geim and K. S. Novoselov, The rise of graphene, *Nat. Mater.*, 2007, **6**, 183.
3 D. Pacile, J. C. Meyer, Ç. Ö. Girit and A. Zettl, The two-dimensional phase of boron nitride: Few-atomic-layer sheets and suspended membranes, *Appl. Phys. Lett.*, 2008, **92**, 133107.
4 W. Q. Han, L. Wu, Y. Zhu, K. Watanabe and T. Taniguchi, Structure of chemically derived mono- and few-atomic-layer boron nitride sheets, *Appl. Phys. Lett.*, 2008, **93**, 223103.
5 K. K. Kim, A. Hsu, X. Jia, S. M. Kim, Y. Shi, M. Hofmann, D. Nezich, J. F. Rodriguez-Nieva, M. Dresselhaus, T. Palacios and J. Kong, Synthesis of Monolayer Hexagonal Boron Nitride on Cu Foil Using Chemical Vapor Deposition, *Nano Lett.*, 2012, **12**, 161.
6 S. Cahangirov, M. Topsakal, E. Aktürk, H. Sahin and S. Ciraci, Two- and One-Dimensional Honeycomb Structures of Silicon and Germanium, *Phys. Rev. Lett.*, 2009, **102**, 236804.
7 P. Vogt, P. De Padova, C. Quaresima, J. Avila, E. Frantzeskakis, M. C. Asensio, A. Resta, B. Ealet and G. Le Lay, Silicene: Compelling Experimental Evidence for Graphenelike Two-Dimensional Silicon, *Phys. Rev. Lett.*, 2012, **108**, 155501.
8 M. E. Davila, L. Xian, S. Cahangirov, A. Rubio and G. L. Lay, Germanene: a novel two-dimensional germanium allotrope akin to graphene and silicene, *New J. Phys.*, 2014, **16**, 095002.
9 R. A. Gordon, D. Yang, E. D. Crozier, D. T. Jiang and R. F. Frindt, Structures of exfoliated single layers of WS_2, MoS_2, and $MoSe_2$ in aqueous suspension, *Phys. Rev. B: Condens. Matter Mater. Phys.*, 2002, **65**, 125407.
10 K. F. Mak, C. Lee, J. Hone, J. Shan and T. F. Heinz, Atomically Thin MoS_2: A New Direct-Gap Semiconductor, *Phys. Rev. Lett.*, 2010, **105**, 136805.
11 J. N. Coleman, M. Lotya, A. O'Neill, S. D. Bergin, P. J. King, U. Khan, K. Young, A. Gaucher, S. De, R. J. Smith, I. V. Shvets, S. K. Arora, G. Stanton, H.-Y. Kim, K. Lee, G. T. Kim, G. S. Duesberg, T. Hallam, J. J. Boland, J. J. Wang, J. F. Donegan, J. C. Grunlan, G. Moriarty, A. Shmeliov, R. J. Nicholls, J. M. Perkins, E. M. Grieveson, K. Theuwissen, D. W. McComb, P. D. Nellist and V. Nicolosi, Two-Dimensional Nanosheets Produced by Liquid Exfoliation of Layered Materials, *Science*, 2011, **331**, 568.
12 Q. H. Wang, K. Kalantar-Zadeh, A. Kis, J. N. Coleman and M. S. Strano, Electronics and optoelectronics of two-dimensional transition metal dichalcogenides, *Nat. Nanotechnol.*, 2012, **7**, 699.
13 H. Sahin, S. Tongay, S. Horzum, W. Fan, J. Zhou, J. Li, J. Wu and F. M. Peeters, Anomalous Raman spectra and thickness-dependent electronic properties of WSe_2, *Phys. Rev. B: Condens. Matter Mater. Phys.*, 2013, **87**, 165409.
14 J. S. Ross, P. Klement, A. M. Jones, N. J. Ghimire, J. Yan, D. G. Mandrus, T. Taniguchi, K. Watanabe, K. Kitamura, W. Yao, D. H. Cobden and X. Xu, Electrically tunable excitonic light-emitting diodes based on monolayer WSe_2 pn junctions, *Nat. Nanotechnol.*, 2014, **9**, 268.
15 B. Chen, H. Sahin, A. Suslu, L. Ding, M. I. Bertoni, F. M. Peeters and S. Tongay, Environmental Changes in $MoTe_2$ Excitonic Dynamics by Defects-Activated Molecular Interaction, *ACS Nano*, 2015, **9**, 5326.
16 F.-F. Zhu, W.-J. Chen, Y. Xu, C.-L. Gao, D.-D. Guan, C.-H. Liu, D. Qian, S.-C. Zhang and J.-F. Jia, Epitaxial growth of two-dimensional stanene, *Nat. Mater.*, 2015, **14**, 1020.
17 S. Saxena, R. P. Chaudhary and S. Shukla, Stanene: Atomically Thick Free-standing Layer of 2D Hexagonal Tin, *Sci. Rep.*, 2016, **6**, 31073.
18 H. Liu, A. T. Neal, Z. Zhu, Z. Luo, X. Xu, D. Tomanek and P. D. Ye, Phosphorene: An Unexplored 2D Semiconductor with a High Hole Mobility, *ACS Nano*, 2014, **8**, 4033.
19 Z. Zhu and D. Tomanek, Semiconducting Layered Blue Phosphorus: A Computational Study, *Phys. Rev. Lett.*, 2014, **112**, 176802.
20 A. Carvalho, M. Wang, X. Zhu, A. S. Rodin, H. Su and A. H. C. Neto, Phosphorene: from theory to applications, *Nat. Rev. Mater.*, 2016, **1**, 16061.
21 W. L. Roth, T. W. DeWitt and A. J. Smith, Polymorphism of Red Phosphorus, *J. Am. Chem. Soc.*, 1947, **69**, 2881.

22 R. Gusmao, Z. Sofer and M. Pumera, Black Phosphorus Rediscovered: From Bulk Material to Monolayers, *Angew. Chem., Int. Ed.*, 2017, **56**, 8052.
23 V. Tran, R. Soklaski, Y. Liang and L. Yang, Layer-controlled band gap and anisotropic excitons in few-layer black phosphorus, *Phys. Rev. B: Condens. Matter Mater. Phys.*, 2014, **89**, 235319.
24 G. Zhang, S. Huang, A. Chaves, C. Song, V. O. Özçelik, T. Low and H. Yan, Infrared fingerprints of few-layer black phosphorus, *Nat. Commun.*, 2017, **8**, 14071.
25 L. Li, Y. Yu, G. J. Ye, Q. Ge, X. Ou, H. Wu, D. Feng, X. H. Chen and Y. Zhang, Black phosphorus field-effect transistors, *Nat. Nanotechnol.*, 2014, **9**, 372.
26 H. Liu, A. T. Neal, Z. Zhu, Z. Luo, X. Xu, D. Tomanek and P. D. Ye, Phosphorene: An Unexplored 2D Semiconductor with a High Hole Mobility, *ACS Nano*, 2014, **8**, 4033.
27 A. S. Rodin, A. Carvalho and A. H. Castro Neto, Strain-Induced Gap Modification in Black Phosphorus, *Phys. Rev. Lett.*, 2014, **112**, 176801.
28 Z. Luo, J. Maassen, Y. Deng, Y. Du, R. P. Garrelts, M. S. Lundstrom, P. D. Ye and X. Xu, Anisotropic in-plane thermal conductivity observed in few-layer black phosphorus, *Nat. Commun.*, 2015, **6**, 8572.
29 Q. Wei and X. Peng, Superior mechanical flexibility of phosphorene and few-layer black phosphorus, *Appl. Phys. Lett.*, 2014, **104**, 251915.
30 X. Peng, Q. Wei and A. Copple, Strain-engineered direct-indirect band gap transition and its mechanism in two-dimensional phosphorene, *Phys. Rev. B: Condens. Matter Mater. Phys.*, 2014, **90**, 085402.
31 Y. Chen, C. Chen, R. Kealhofer, H. Liu, Z. Yuan, L. Jiang, J. Suh, J. Park, C. Ko, H. S. Choe, J. Avila, M. Zhong, Z. Wei, J. Li, S. Li, H. Gao, Y. Liu, J. Analytis, Q. Xia, M. C. Asensio and J. Wu, Black Arsenic: A Layered Semiconductor with Extreme InPlane Anisotropy, *Adv. Mater.*, 2018, **30**, 1800754.
32 H.-S. Tsai, S.-W. Wang, C.-H. Hsiao, C.-W. Chen, H. Ouyang, Y.-L. Chueh, H.-C. Kuo and J.-H. Liang, Direct Synthesis and Practical Bandgap Estimation of Multilayer Arsenene Nanoribbons, *Chem. Mater.*, 2016, **28**, 425.
33 C. Kamal and M. Ezawa, Arsenene: Two-dimensional buckled and puckered honeycomb arsenic systems, *Phys. Rev. B: Condens. Matter Mater. Phys.*, 2015, **91**, 085423.
34 Z. Zhu, J. Guan and D. Tomanek, Strain-induced metal-semiconductor transition in monolayers and bilayers of gray arsenic: A computational study, *Phys. Rev. B: Condens. Matter Mater. Phys.*, 2015, **91**, 161404(R).
35 S. Zhang, Z. Yan, Y. Li, Z. Chen and H. Zeng, Atomically thin arsenene and antimonene: semimetalsemiconductor and indirectdirect bandgap transitions, *Angew. Chem., Int. Ed.*, 2015, **54**, 3112.
36 S. Zhang, M. Xie, F. Li, Z. Yan, Z. Chen and H. Zeng, Semiconducting group 15 monolayers: a broad range of band gaps and high carrier mobilities, *Angew. Chem., Int. Ed.*, 2016, **55**, 1666.
37 R. Gusmao, Z. Sofer, D. Bousa and M. Pumera, Pnictogen (As, Sb, Bi) Nanosheets for Electrochemical Applications Are Produced by Shear Exfoliation Using Kitchen Blenders, *Angew. Chem., Int. Ed.*, 2017, **56**, 14417.
38 O. Osters, T. Nilges, F. Bachhuber, F. Pielnhofer, R. Weihrich, M. Schöneich and P. Schmidt, Synthesis and Identification of Metastable Compounds: Black Arsenic Science or Fiction?, *Angew. Chem., Int. Ed.*, 2012, **51**, 2994.
39 C. Wang, Q. Xia, Y. Nie, M. Rahman and G. Guo, Strain engineering band gap, effective mass and anisotropic Dirac-like cone in monolayer arsenene, *AIP Adv.*, 2016, **6**, 035204.
40 G. Moynihan, S. Sanvito and D. O'Regan, Strain-induced Weyl and Dirac states and direct-indirect gap transitions in group-V materials, *2D Mater.*, 2017, **4**, 045018.
41 H. B. Ribeiro, M. A. Pimenta, C. J. S. de Matos, R. L. Moreira, A. S. Rodin, J. D. Zapata, E. A. T. de Souza and A. H. Castro Neto, Unusual Angular Dependence of the Raman Response in Black Phosphorus, *ACS Nano*, 2015, **9**, 4270.
42 H. B. Ribeiro, M. A. Pimenta and C. J. S. de Matos, Raman spectroscopy in black phosphorus, *J. Raman Spectrosc.*, 2018, **49**, 76.
43 G. Kresse and D. Joubert, From ultrasoft pseudopotentials to the projector augmented-wave method, *Phys. Rev. B: Condens. Matter Mater. Phys.*, 1999, **59**, 1758.
44 G. Kresse and J. Hafner, Ab initio molecular dynamics for liquid metals, *Phys. Rev. B: Condens. Matter Mater. Phys.*, 1993, **47**, 558.
45 G. Kresse and J. Furthmuller, Efficient iterative schemes for ab initio total-energy calculations using a plane-wave basis set, *Phys. Rev. B: Condens. Matter Mater. Phys.*, 1996, **54**, 11169.
46 J. P. Perdew, K. Burke and M. Ernzerhof, Generalized Gradient Approximation Made Simple, *Phys. Rev. Lett.*, 1996, **77**, 3865.
47 S. J. Grimme, Semiempirical GGAtype density functional constructed with a longrange dispersion correction, *Comput. Chem.*, 2006, **27**, 1787.
48 A. Togo, F. Oba and I. Tanaka, First-principles calculations of the ferroelastic transition between rutile-type and $CaCl_2$-type SiO_2 at high pressures, *Phys. Rev. B: Condens. Matter Mater. Phys.*, 2008, **78**, 134106.
49 K. Parlinski, Z. Q. Li and Y. Kawazoe, First-Principles Determination of the Soft Mode in Cubic ZrO_2, *Phys. Rev. Lett.*, 1997, **78**, 4063.
50 D. Kecik, E. Durgun and S. Ciraci, Stability of single-layer and multilayer arsenene and their mechanical and electronic properties, *Phys. Rev. B*, 2016, **94**, 205409.
51 J.-W. Jiang and H. S. Park, Negative poissons ratio in single-layer black phosphorus, *Nat. Commun.*, 2014, **5**, 4727.
52 Z. S. Popović, J. M. Kurdestany and S. Satpathy, Electronic structure and anisotropic Rashba spin-orbit coupling in monolayer black phosphorus, *Phys. Rev. B: Condens. Matter Mater. Phys.*, 2015, **92**, 035135.
53 X. Wang, A. M. Jones, K. L. Seyler, V. Tran, Y. Jia, H. Zhao, H. Wang, L. Yang, X. Xu and F. Xia, Highly anisotropic and robust excitons in monolayer black phosphorus, *Nat. Nanotechnol.*, 2015, **10**, 517.
54 J. Kang, H. Sahin and F. M. Peeters, Mechanical properties of monolayer sulphides: a comparative study between MoS_2, HfS_2 and TiS_3, *Phys. Chem. Chem. Phys.*, 2015, **17**, 27742.
55 W. Zhang, J. Yin, P. Zhang and Y. Ding, Strain/stress engineering on the mechanical and electronic properties of phosphorene nanosheets and nanotubes, *RSC Adv.*, 2017, **7**, 51466.

56 C. E. P. Villegas, A. R. Rocha and A. Marini, Anomalous Temperature Dependence of the Band Gap in Black Phosphorus, *Nano Lett.*, 2016, **16**, 5095.

57 M. Yagmurcukardes, C. Bacaksiz, E. Unsal, B. Akbali, R. T. Senger and H. Sahin, Strain mapping in single-layer two-dimensional crystals via Raman activity, *Phys. Rev. B*, 2018, **97**, 115427.

58 G. Placzek, in *Rayleigh-Streuung und Raman-Effekt*, ed. E. Marx, Handbuch der Radiologie, Academische Verlag, Leipzig, 1934, vol. 6, p. 205.

59 C. H. Chang, X. F. Fan, S. H. Lin and J. L. Kuo, Orbital analysis of electronic structure and phonon dispersion in MoS_2, $MoSe_2$, WS_2, and WSe_2 monolayers under strain, *Phys. Rev. B: Condens. Matter Mater. Phys.*, 2013, **88**, 195420.

60 C. R. Zhu, G. Wang, B. L. Liu, X. Marie, X. F. Qiao, X. Zhang, X. X. Wu, H. Fan, P. H. Tan, T. Amand and B. Urbaszek, Strain tuning of optical emission energy and polarization in monolayer and bilayer MoS_2, *Phys. Rev. B: Condens. Matter Mater. Phys.*, 2013, **88**, 121301.

